

Extremely large magnetoresistance and high-density Dirac-like fermions in ZrB₂Qi Wang (王琦), Peng-Jie Guo (郭朋杰), Shanshan Sun (孙珊珊), Chenghe Li (李承贺), Kai Liu (刘凯),*
Zhong-Yi Lu (卢仲毅), and Hechang Lei (雷和畅)[†]*Department of Physics and Beijing Key Laboratory of Opto-electronic Functional Materials & Micro-nano Devices,
Renmin University of China, Beijing 100872, China*

(Received 9 December 2017; published 7 May 2018)

We report the detailed study on transport properties of ZrB₂ single crystal, a predicted topological nodal-line semimetal. ZrB₂ exhibits extremely large magnetoresistance as well as field-induced resistivity upturn and plateau. These behaviors can be well understood by the two-band model with the perfect electron-hole compensation and high carrier mobilities. More importantly, the electrons with small effective masses and nontrivial Berry phase have significantly high density when compared to those in known topological semimetals. It strongly suggests that ZrB₂ hosts Dirac-like nodal-line fermions.

DOI: [10.1103/PhysRevB.97.205105](https://doi.org/10.1103/PhysRevB.97.205105)

Recently discovered topological semimetals (TSMs), as a new kind of gapless-type topological quantum materials, have induced extensive research interest because of exotic physical phenomena and potential applications for novel devices. TSMs are characterized by the robust bulk band crossings (nodal points) near Fermi energy level E_F [1–4]. Due to the novel bulk and surface topological band structures, TSMs exhibit many exotic transport and spectroscopic properties. For example, there are linear dispersions around band crossing points with unusual quasiparticle excitations behaving like Dirac or Weyl fermions in high-energy physics [4–10]. Moreover, TSMs host novel topological surface states (SSs), such as the Fermi arc and the drumhead SSs [2,3,8–14]. They also exhibit extremely large magnetoresistance (XMR) with ultrahigh carrier mobility [15,16], and chiral anomalies with negative longitudinal MR [17,18].

According to the momentum space distribution and degeneracy of the nodal points, the TSMs can be classified into two types. The first class of TSMs has zero-dimensional (0D) discrete nodal points, such as fourfold-degenerate Dirac points [4–7], twofold-degenerate Weyl points [8–10], etc. In contrast, there is a line along which two bands cross each other in the Brillouin zone in the second class, namely, topological nodal-line semimetals (TNLSMs) [1,12]. One-dimensional (1D) nodal lines can connect to each other to form a nodal ring, nodal chain, or nodal net [19,20]. Many materials have been proposed as candidates of TNLSMs in theory, such as all-carbon Mackay-Terrones crystals [12], Cu₃PdN [13], PbTaSe₂ [14], IrF₄ [20], Ca₃P₂ [21,22], ZrSiCh ($Ch = S, Se, \text{ and } Te$) [23,24], CaAgX ($X = P \text{ and } As$) [25–27], etc. However, the bulk nodal-ring states and drumhead SSs have only been observed in limited materials, such as PbTaSe₂, ZrSiCh, CaAgX, etc. [14,23,26,27]. The nodal-chain and nodal-net states are still elusive.

Very recently, first-principles calculations predict that AlB₂-type diborides MB_2 ($M = Sc, Ti, V, Zr, Hf, Nb, \text{ and}$

Ta) could be a new family of TNLSMs, which can host a nodal ring and nodal net with threefold-degenerate points when spin-orbit coupling (SOC) is ignored [28,29]. Moreover, these materials have larger energy ranges of linear dispersion ($> 2 \text{ eV}$) than other TSMs [28,29], in favor of the experimental study. Stimulated by these theoretical studies, in this work, we perform a detailed study on the magnetotransport properties of ZrB₂ single crystals. ZrB₂ exhibits XMR as well as significant field-induced resistivity upturn and plateau at low temperature. Experimental and theoretical results further indicate that there are two sets of three-dimensional (3D) Fermi surfaces (FSs) with nearly compensated carrier densities. These carriers exhibit high mobilities, light effective masses, and nontrivial Berry phase. More importantly, the carrier densities in ZrB₂ are much higher than those in most of TSMs—even the TNLSM ZrSiCh.

Single crystals of ZrB₂ were grown by the Fe flux method (details are presented in the Supplemental Material [30]). X-ray diffraction (XRD) of a single crystal was performed using a Bruker D8 x-ray machine with Cu $K\alpha$ radiation. The elemental analysis was performed using energy-dispersive x-ray (EDX) spectroscopy analysis. Electrical transport measurements were carried out by using Quantum Design PPMS-14T. The longitudinal and Hall electrical resistivity were measured by using a standard four-probe method. The electronic structures of ZrB₂ were studied by using first-principles calculations [30].

ZrB₂ adopts an AlB₂-type centrosymmetric structure with the space group $P6/mmm$ (No. 191). The B atoms form graphenelike hexagon planes along the ab plane and Zr atoms are located between two B layers [inset of Fig. 1(a)]. The powder XRD pattern confirms the pure phase of the ZrB₂ sample and the fitted lattice parameters are $a = 3.1692(1) \text{ \AA}$ and $c = 3.5307(2) \text{ \AA}$ (Fig. S1 in the Supplemental Material [30]), close to the reported values in the literature [31]. Moreover, both the powder XRD pattern and the EDX spectrum (Fig. S2 in the Supplemental Material [30]) indicate that the ZrB₂ single crystals are free from flux. The XRD pattern of a ZrB₂ single crystal indicates that the surface of the crystal is the (00 l) plane [Fig. 1(a)]. The hexagon shape of the ZrB₂

*kliu@ruc.edu.cn

[†]hlel@ruc.edu.cn

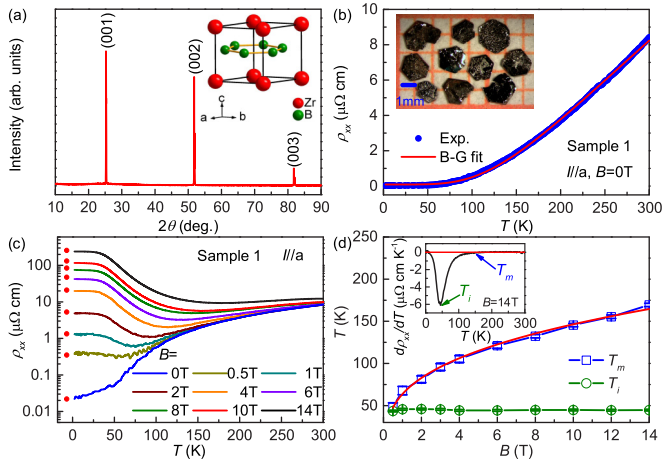


FIG. 1. (a) XRD of a ZrB_2 single crystal. Inset: crystal structure of ZrB_2 . (b) Temperature dependence of zero-field $\rho_{xx}(T,0)$ for $I||a$, fitted using the B-G formula. Inset: photo of typical ZrB_2 single crystals. (c) Temperature dependence of $\rho_{xx}(T,B)$ at various fields. The red solid points are obtained from the formula $\rho_0 + \alpha B^2/\rho_0$, where α is fitted from the MR curve at 2 K. (d) Field dependence of T_m and T_i , corresponding to the sign change and the minimum in the $d\rho_{xx}(T,B)/dT$ curves, respectively. The red solid line is the fit using $T_m(B) \propto (B - B_c)^{1/n}$ where $B_c = \rho_0/\alpha^{1/2}$. Inset: $d\rho_{xx}(T,B)/dT$ vs T at 14 T. The positions of T_m and T_i are marked by arrows.

crystal [inset of Fig. 1(b)] is consistent with the single-crystal XRD pattern and its crystallographic symmetry. The zero-field in-plane resistivity $\rho_{xx}(T,0)$ of the ZrB_2 single crystal exhibits good metallic behavior and the rather large residual resistance ratio [RRR $\equiv \rho_{xx}(300\text{ K})/\rho_{xx}(2\text{ K}) \simeq 386$] indicates the high quality of crystals [Fig. 1(b)]. Previous studies indicate that the e - ph scattering is dominant in ZrB_2 [32,33], similar to MgB_2 , a typical material with a strong e - ph interaction. According to the Bloch-Grüneisen (B-G) formula [34],

$$\rho_{xx}(T) = \rho_0 + C \left(\frac{T}{\Theta_D} \right)^5 \int_0^{\Theta_D/T} \frac{x^5}{(e^x - 1)(1 - e^{-x})} dx, \quad (1)$$

where ρ_0 is the residual resistivity, Θ_D is the Debye temperature, and C is a constant. The good fit of the $\rho_{xx}(T)$ curve over the full temperature range [red solid line in Fig. 1(b)] shows that the e - ph scattering is dominant in ZrB_2 . The fitted Θ_D is 779(3) K, close to the values derived from ZrB_2 polycrystal [32]. Such high Debye temperature can be ascribed to the vibration of B atoms with light mass.

When applying a magnetic field, the $\rho_{xx}(T,B)$ curve exhibits a clearly upturn behavior [Fig. 1(c)]. Even at a very small field of 0.5 T, the slope of the $\rho_{xx}(T,B)$ curve shows a sign change from positive at high temperature to negative at low temperature, i.e., there is a minimum in the $\rho_{xx}(T,B)$ curve at “turn-on” temperature $T_m(B)$ [inset of Fig. 1(d)]. With increasing the field, the $T_m(B)$ gradually shifts to higher temperature [Fig. 1(d)]. On the other hand, there is a plateau in the $\rho_{xx}(T,B)$ curve following the upturn behavior at low temperatures and high fields. The temperature at which the resistivity plateau begins to appear seems unchanged with fields. It can be seen more clearly from the field dependence of the characteristic temperature $T_i(B)$ related to the inflection

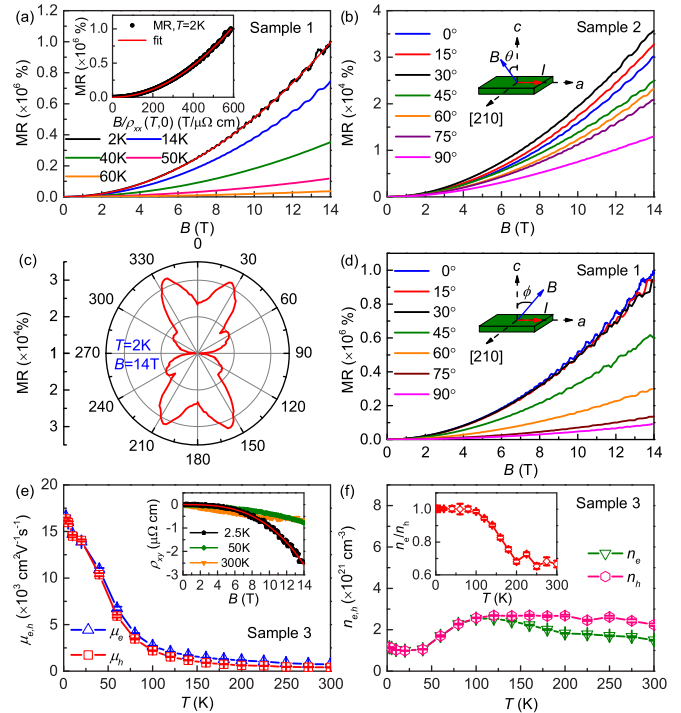


FIG. 2. (a) Field dependence of MR at various temperatures. The red solid line is the fit using the $\text{MR} \propto B^m$ at 2 K. Inset: the relation between MR and $B/\rho_{xx}(T,0)$ at $T = 2\text{ K}$. The red solid line shows the fit using $\text{MR} = \alpha [B/\rho_{xx}(T,0)]^2$. (b) Field dependence of MR at 2 K with the field rotating from the c axis to the ab plane. The field is always perpendicular to the current direction ($I||a$). (c) Polar plot of AMR at 2 K and 14 T. (d) Field dependence of MR at 2 K with the field tilting from the c axis to the current direction (a axis). (e) Temperature dependence of fitted carrier mobilities $\mu_{e,h}(T)$. Inset: field dependence of $\rho_{xy}(T,B)$ at several typical temperatures. The red solid line is the fit using the two-band model. (f) Temperature dependence of fitted carrier concentrations $n_{e,h}(T)$. Inset: the ratio of n_e/n_h as a function of temperature.

point of the $\rho_{xx}(T,B)$ curve [inset of Fig. 1(d)]. As shown in Fig. 1(d), the $T_i(B)$ is about 45 K when $B > 1\text{ T}$ and almost insensitive to the field.

ZrB_2 exhibits significantly large MR ($= [\rho_{xx}(T,B) - \rho_{xx}(T,0)]/\rho_{xx}(T,0) \times 100\%$) at low temperature. The MR at 2 K reaches $4.2 \times 10^5\%$ and $1.0 \times 10^6\%$ at 9 and 14 T for $H||c$ [Fig. 2(a)], comparable to the MRs in other TSMs and compensated semimetals (SMs) [15–17,35–37]. Moreover, the MR does not saturate up to 14 T and the Shubnikov–de Haas (SdH) quantum oscillations (QOs) appear at the low-temperature and high-field region [Fig. 2(a)]. The MR at 2 K can be well fitted using the formula $\text{MR} \propto B^m$ with $m = 1.989(4)$ [Fig. 2(a)], very close to the typically quadratic field dependence of the MR in the multiband compensated metals [34]. The MR decreases gradually with increasing temperature, but it is still unsaturated up to 14 T even at 300 K. As shown in Fig. 2(b), when the field rotates away from the c axis toward the ab plane ($\theta = 0^\circ$ corresponding to $B||c$), the MR at 14 T increases at first and then decreases. Finally, it reaches a minimum value at $\theta = 90^\circ$ ($B||ab \perp I$). This complex angular-resolved magnetoresistance (AMR) behavior can be seen more clearly

on the polar plot of AMR at 2 K and 14 T [Fig. 2(c)]. There are multiple local maximum and minimum values on the plot and the maximum value appears at $\theta \sim 26^\circ$. Similar behaviors have been observed previously when the field is relatively low [38]. This reflects the large anisotropy of FSs and/or relaxation times. The field dependence of MR is unsaturated for all of the field directions, the exponent m varies slightly from 1.7 to 2 (Table S1 and Fig. S3 in the Supplemental Material [30]). The SdH QOs can be observed for all of the field directions. When the field is tilting from $B \parallel c \perp I$ ($\phi = 0^\circ$) to $B \parallel a \parallel I$ ($\phi = 90^\circ$), the MR at 2 K and 14 T has a maximum value for $\phi = 0^\circ$ and decreases monotonically [Fig. 2(d)]. However, there is no negative longitudinal MR observed when $B \parallel I$ ($\phi = 90^\circ$). Similar to the MR curves in Fig. 2(b), the derived m of the curves in Fig. 2(d) are also close to 2 with slight deviations (Table S2 and Fig. S4 in the Supplemental Material [30]). On the other hand, the MR with $I \parallel [210]$ (rotating 90° from the a axis in the ab plane) exhibits similar field dependence to those with $I \parallel a$ (Table S3 and Fig. S5 in the Supplemental Material [30]). Thus, the MR is insensitive to the current direction rotated in the ab plane. In addition, the negative longitudinal MR is still absent when $I \parallel [210]$.

The inset of Fig. 2(e) shows the field dependence of Hall resistivity $\rho_{xy}(T, B)$ at various temperatures. The $\rho_{xy}(T, B)$ at high temperature has a nearly linear dependence on field; when decreasing temperature, the $\rho_{xy}(T, B)$ bends downward at high field. The nonlinear behavior clearly indicates that ZrB_2 is a multiband metal. Moreover, the QOs can be seen at the low-temperature and high-field region, consistent with the MR results. Using the two-band model [34],

$$\rho_{xx} = \frac{1}{e} \frac{(n_h \mu_h + n_e \mu_e) + (n_h \mu_e + n_e \mu_h) \mu_h \mu_e B^2}{(n_h \mu_h + n_e \mu_e)^2 + (n_h - n_e)^2 (\mu_e \mu_h)^2 B^2}, \quad (2)$$

$$\rho_{xy} = \frac{B}{e} \frac{(n_h \mu_h^2 - n_e \mu_e^2) + (n_h - n_e) (\mu_e \mu_h)^2 B^2}{(n_h \mu_h + n_e \mu_e)^2 + (n_h - n_e)^2 (\mu_e \mu_h)^2 B^2}, \quad (3)$$

where $\mu_{e,h}$ and $n_{e,h}$ are the mobilities and concentrations of electron- and hole-type carriers, respectively. The $\rho_{xx}(T, B)$ and $\rho_{xy}(T, B)$ can be fitted very well [red solid line in the inset of Fig. 2(e) and Fig. S6 in the Supplemental Material [30]] and the obtained $\mu_{e,h}(T)$ and $n_{e,h}(T)$ as a function of temperature are shown in Figs. 2(e) and 2(f). The $\mu_{e,h}(T)$ exhibits similar temperature dependence, i.e., monotonically decreases with similar slopes when increasing temperature [Fig. 2(e)], reflecting a similar e - ph scattering mechanism for both types of carriers. At high temperature, μ_e is about twice larger than μ_h and both of them become rather high at low temperature [$1.66(1)$ and $1.64(1) \times 10^4 \text{ cm}^2 \text{ V}^{-1} \text{ s}^{-1}$ for μ_e and μ_h at 2 K, respectively]. On the other hand, when $T < 125$ K, the $n_{e,h}(T)$ are almost the same and increase gradually with temperature [Fig. 2(f)]. The estimated n_e and n_h at 2 K are $1.156(5)$ and $1.153(5) \times 10^{21} \text{ cm}^{-3}$. Correspondingly, the ratio of n_e/n_h at 2 K is very close to one [1.003(9)] with tiny amounts of excess n_e compared to n_h [inset of Fig. 2(f)]. This undoubtedly indicates that the carriers in ZrB_2 are nearly compensated at low temperature. In contrast, when $T > 125$ K, the $n_e(T)$ starts to decrease while the $n_h(T)$ still keeps increasing until about 200 K, leading to the gradual decrease of the ratio of n_e/n_h . As to the above exponent m , because of the nearly perfect compensation of electrons and holes, the B^2 term in

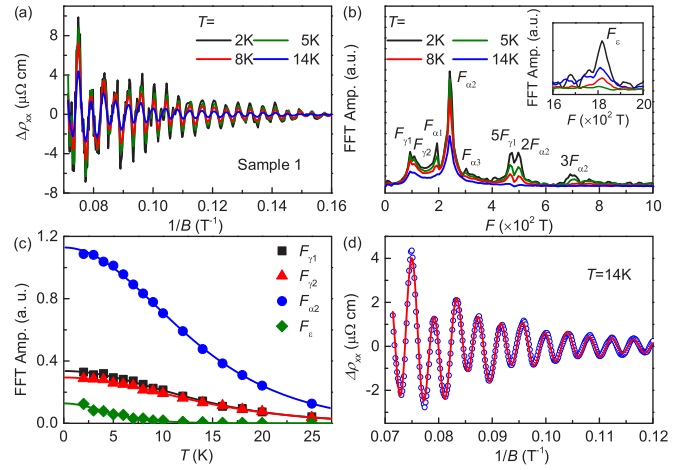


FIG. 3. (a) SdH QOs $\Delta\rho_{xx} = \rho_{xx} - \langle\rho_{xx}\rangle$ as a function of $1/B$ at various temperatures for $B \parallel c$. (b) FFT spectra of the QOs at various temperatures. Inset: FFT spectra at high-frequency region. (c) The temperature dependence of FFT amplitudes of $F_{\gamma 1}$, $F_{\gamma 2}$, $F_{\alpha 2}$, and F_{ϵ} peaks. The solid lines represent the L-K formula fits for m^* . (d) Two-band L-K formula fit (red solid line) of SdH QO (blue empty circles) at $T = 14$ K.

the denominator of Eq. (2) would have some contributions to the MR, leading to the slight deviation of m from 2. Moreover, the μ_e and μ_h are related to the relaxation times which are sensitive to the directions of field and current; the changes of the B^2 term could lead to the variations of m for different field and/or current directions (Tables S1– S3 and Figs. S2– S4 in the Supplemental Material [30]), especially for the complicated Fermi surfaces as in ZrB_2 . On the other hand, such small variations of m for different field and current orientations may also result from the misalignment and shape of the voltage leads. For the non-point-contact potential lead, it may act like an electrical short over the region of contact perturbing the current distribution and leads to the deviation of m from 2 [39].

Analysis of SdH QOs provides further insight on the features of FSs and carriers. The oscillation parts of resistivity $\Delta\rho_{xx} = \rho_{xx} - \langle\rho_{xx}\rangle$ against the reciprocal of magnetic field $1/B$ for $B \parallel c$ at several representative temperatures are shown in Fig. 3(a). The amplitudes of QOs exhibit complex periodic behaviors, indicating the contributions of multiple frequency components. They decrease with increasing temperature or decreasing field, but still persist up to about 20 K. The fast Fourier transform (FFT) spectra of SdH QOs for $B \parallel c$ reveal several fundamental frequencies $F_{\gamma 1} = 93.2$ T, $F_{\gamma 2} = 108.8$ T, $F_{\alpha 1} = 194.2$ T, $F_{\alpha 2} = 240.8$ T, $F_{\alpha 3} = 303.0$ T, and $F_{\epsilon} = 1817.7$ T, and their corresponding higher harmonic frequencies [main panel and inset of Fig. 3(b)]. These frequencies are well consistent with the results derived from the de Haas–van Alphen QOs [40,41]. According to the Onsager relation $F = (\hbar/2\pi e)A_F$, where A_F is the area of extremal orbit of FS. The determined A_F is 0.0089–0.0104, 0.0185–0.0289, and 0.1733 \AA^{-2} for the γ , α , and ϵ extremal orbits, respectively. The A_F 's of the γ and α frequencies are relatively small when compared to that of the ϵ frequency. The former takes about 0.26%–0.30% and 0.54%–0.85%, and the latter occupies about

5.09% of the whole area of Brillouin zone in the k_x - k_y plane providing the lattice parameter $a = 3.1692$ Å. In general, the SdH QOs with several frequencies can be described by linear superposition of the multifrequency Lifshitz-Kosevich (L-K) formula, each of which can be expressed as [24,42–44]

$$\Delta\rho_{xx}^i \propto \frac{5}{2} \sqrt{\frac{B}{2F}} R_T R_D R_S \cos[2\pi(F/B + \gamma - \delta + \varphi)], \quad (4)$$

where for the i th SdH QO component, F is frequency, $R_T = (\lambda m^* T/B)/\sinh(\lambda m^* T/B)$, $R_D = \exp(-\lambda m^* T_D/B)$, $R_S = \cos(\pi m^* g^*)$, m^* is effective cyclotron mass in unit of free electron mass m_0 , T_D is the Dingle temperature, g^* is the effective g factor, and constant $\lambda = 2\pi^2 k_B m_0 / e\hbar \approx 14.7$ T/K. The phase factor $\gamma - \delta + \varphi$ contains $\gamma = 1/2 - \phi_B/2\pi$ where ϕ_B is Berry phase, δ is determined by the dimensionality of FS ($\delta = 0$ and $\pm 1/8$ for the two-dimensional and 3D cases) [42,45,46], and $\varphi = 1/2$ ($\rho_{xx} \gg \rho_{xy}$) or 0 ($\rho_{xx} \ll \rho_{xy}$) [47]. First, the m^* 's are obtained by fitting the temperature dependence of the FFT amplitudes to the R_T [48]. The fitted m^* is 0.112(1), 0.107(1), 0.1126(7), and 0.29(1) m_0 for $F_{\gamma 1}$, $F_{\gamma 2}$, $F_{\alpha 2}$ and F_ε , respectively [Fig. 3(c)]. Setting the obtained m^* as a known parameter, the precise values of ϕ_B and T_D 's can be obtained from the fit of SdH QOs using the multifrequency L-K formula. Here we focus on the low-frequency QO components because of the relatively low measuring field limits to get reliable values of ϕ_B and T_D for the high-frequency F_ε . In addition, in order to minimize the influences of Zeeman splitting and harmonic frequencies, the SdH QO at 14 K is fitted. The two-frequency L-K formula can describe the SdH QO quite well [Fig. 3(d)]. The fitted T_D are 47(2) and 20.9(4) K for F_γ (average of $F_{\gamma 1}$ and $F_{\gamma 2}$) and $F_{\alpha 2}$, corresponding to the quantum mobilities $\mu_Q = \frac{e\hbar}{2\pi k_B m^* T_D} = 4.2(2) \times 10^2$ and $9.1(2) \times 10^2$ cm² V⁻¹ s⁻¹. The μ_Q is smaller than the μ_e because the former is sensitive to both large- and small-angle scattering, whereas the latter is affected by only large-angle scattering [42]. Because of $\rho_{xx} \gg \rho_{xy}$ and a strong 3D character of FSs in ZrB₂ (shown below), we take $\varphi = 1/2$ and $\delta = \pm 1/8$. Based on these values, the fitted ϕ_B are $0.583(5)\pi$ ($\delta = 1/8$) and $1.083(5)\pi$ ($\delta = -1/8$) for F_γ , and $0.005(2)\pi$ ($\delta = 1/8$) and $0.505(2)\pi$ ($\delta = -1/8$) for $F_{\alpha 2}$. Thus, there is a nontrivial ϕ_B for F_γ . The variation of ϕ_B at different extremal orbits of the same electron pocket (shown below) could be related to the anisotropy of FS. Similar behavior has been observed in TNLSM ZrSiCh [24]. Moreover, it has to be noted that when the Berry phase is not included ($\phi_B = 0$), the SdH QO cannot be well fitted by the two-frequency L-K formula (Fig. S7 in the Supplemental Material [30]). It indicates that a nontrivial Berry phase must be taken into account in order to correctly describe the experimental results, therefore confirming the topological nature of ZrB₂.

Theoretical calculations show that there are two bands crossing the E_F for ZrB₂ [Fig. 4(a)]. The electron-type FS surrounds the nodal rings in the Γ - M - K and Γ - K - H planes, which connect to each other around the K points and form a nodal net [Fig. 4(b)]. This is consistent with previous calculations [28,29]. The complex 3D electron FS could be the origin of the strong anisotropy of MR [Fig. 2(b)]. When the SOC is included, small energy gaps (~ 40 – 60 meV) open around the nodal net [Fig. 4(c)], but the dispersions of the electron band are still linear in a wide energy range up to 3 eV around the

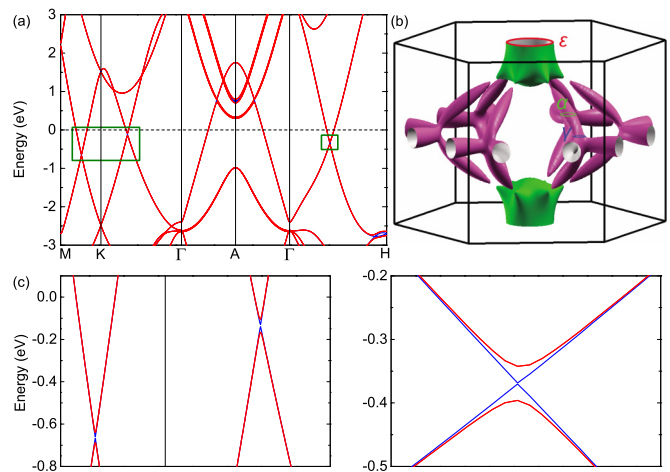


FIG. 4. (a) Band structure of ZrB₂ calculated without (blue) and with (red) the SOC effect. The horizontal dashed line denotes the position of E_F . (b) Calculated electron-type FS around the K point and hole-type FS around the A point. The extremal orbits observed in the SdH QOs are labeled. (c) Enlarged regions of band structure labeled using green boxes in (a).

E_F [Fig. 4(a)], indicating Dirac-like fermions with high carrier mobilities existing in ZrB₂. The hole pocket is located at the A point showing a 3D cylinderlike FS with the long principle axis along the Γ - A direction. The α and γ frequencies in the SdH QO measurements [Fig. 3(a)] can be ascribed to the extremal orbits of electron pockets while the ε frequency corresponds to that of the hole pocket [Fig. 4(b)] [40,41]. Based on the volume information of electron and hole pockets, the calculated concentrations of electron- and hole-type carriers $n_{e,h}$ are 1.32 and 1.27×10^{21} cm⁻³, which are in good agreement with the results of Hall measurements. The calculations once again confirm that ZrB₂ is a compensated semimetal ($n_e/n_h = 1.04$) with relatively high carrier densities.

The field-induced resistivity upturn and plateau behaviors have been frequently observed in TSMs and compensated SMs, such as NbP, WTe₂, LaSb/LaBi, ZrSiS, etc. [16,35–37,49]. Several mechanisms have been proposed to explain these behaviors, such as perfect electron-hole compensation [37,50,51] and field-induced gap opening at the Weyl (Dirac) points [16,52]. The following analysis strongly implies that the large MR and field-induced behaviors in ZrB₂ can be explained well by the two-band model with the electron-hole compensated condition and high carrier mobilities. According to the two-band model with the condition of carrier compensation ($n_e = n_h$) [34,37,50], first, the MR = $\mu_e \mu_h B^2 = \alpha [B/\rho_{xx}(T,0)]^2$. Thus, the field dependence of MR is quadratic [inset of Fig. 2(a)] and the large MR is directly related to the high $\mu_{e,h}$ in ZrB₂ at low temperature. At high temperature, combined with the quick decreases of $\mu_{e,h}$ and the uncompensated carriers, the MR at high temperature becomes much smaller than that at low temperature. Second, there should be a minimum in the $\rho_{xx}(T,B)$ curve when $B > B_c (= \rho_0/\alpha^{1/2})$ [37,50], i.e., field-induced resistivity upturn. Using $\rho_{xx}(T = 2 \text{ K}, 0) = 0.022 \mu\Omega \text{ cm}$ and fitted $\alpha = 0.029 (\mu\Omega \text{ cm/T})^2$ [inset of Fig. 2(a)], the determined B_c is about 0.13 T, well consistent with the resistivity minimum appearing when

$B > 0.5$ T [Fig. 1(c)]. Third, a resistivity plateau with the value of $\rho_0 + \alpha B^2/\rho_0$ should appear at low temperature [37]. As shown in Fig. 1(c), the derived values of resistivity plateau (red solid points) is in good agreement with the experimental values at 2 K. Fourth, if the $\rho_{xx}(T, 0)$ can be described approximately by the formula $\rho_0 + AT^n$, the $T_m(B)$ should be proportional to $(B - B_c)^{1/n}$ [37]. Providing the B_c is 0.13 T, the fitted n is 2.92(8) [Fig. 1(d)], very close to the fitted n [= 2.92(2)] from the $\rho_{xx}(T, 0)$ curve between 2 and 170 K [corresponding to the $T_m(B)$ at $B = 14$ T] (Fig. S8 in the Supplemental Material [30]).

The high $\mu_{e,h}$ in ZrB₂ could be partially ascribed to the small m^* 's. Such small m^* 's are comparable with those in the known TSMs [15, 16, 24]. In contrast, the $n_{e,h}$ in ZrB₂ are much higher than those in the TSMs with discrete nodal points ($\sim 10^{17}$ – 10^{18} cm⁻³) [15, 18], and even larger than those of TNLSM ZrSiCh ($\sim 10^{20}$ cm⁻³) [24]. Combined with the nontrivial ϕ_B of the electron pocket, it strongly suggests that the electron-type carriers in ZrB₂ have the feature of Dirac-like nodal-line fermions.

In summary, ZrB₂ exhibits XMR and field-induced exotic phenomena at low temperature. The nearly perfect electron-hole compensation and remarkably high mobilities

$\mu_{e,h}$ are the essential conditions leading to these exotic phenomena. More importantly, ZrB₂ has very large $n_{e,h}$ with significantly small m^* 's and nontrivial ϕ_B , especially for the electron band. This strongly implies that there are Dirac-like nodal-line fermions in ZrB₂. Even when there are high-density carriers, the small m^* 's of Dirac-like fermions can still result in very high $\mu_{e,h}$, a prerequisite for the XMR behavior. Thus, the current work will shed light on exploring novel XMR materials in a broader scope, other than semimetals with low carrier concentrations.

This work was supported by the National Key R&D Program of China (Grants No. 2016YFA0300504 and No. 2017YFA0302903), the National Natural Science Foundation of China (Grants No. 11474356, No. 11574394, No. 11774423, No. 11774424, and No. 91421304), and the Fundamental Research Funds for the Central Universities, and the Research Funds of Renmin University of China (RUC) (Grants No. 14XNLQ03, No. 15XNLF06, No. 15XNLQ07, and No. 16XNLQ01). Computational resources were provided by the Physical Laboratory of High Performance Computing at Renmin University of China.

Q.W. and P.-J.G. contributed equally to this work.

-
- [1] A. A. Burkov, M. D. Hook, and L. Balents, *Phys. Rev. B* **84**, 235126 (2011).
- [2] G. Xu, H. Weng, Z. Wang, X. Dai, and Z. Fang, *Phys. Rev. Lett.* **107**, 186806 (2011).
- [3] X. Wan, A. M. Turner, A. Vishwanath, and S. Y. Savrasov, *Phys. Rev. B* **83**, 205101 (2011).
- [4] Z. Wang, Y. Sun, X.-Q. Chen, C. Franchini, G. Xu, H. Weng, X. Dai, and Z. Fang, *Phys. Rev. B* **85**, 195320 (2012).
- [5] Z. Wang, H. Weng, Q. Wu, X. Dai, and Z. Fang, *Phys. Rev. B* **88**, 125427 (2013).
- [6] Z. K. Liu, B. Zhou, Y. Zhang, Z. J. Wang, H. Weng, D. Prabhakaran, S.-K. Mo, Z. X. Shen, Z. Fang, X. Dai, Z. Hussain, and Y. L. Chen, *Science* **343**, 864 (2014).
- [7] Z. K. Liu, J. Jiang, B. Zhou, Z. J. Wang, Y. Zhang, H. M. Weng, D. Prabhakaran, S. K. Mo, H. Peng, P. Dudin, T. Kim, M. Hoesch, Z. Fang, X. Dai, Z.-X. Shen, D. L. Feng, Z. Hussain, and Y. L. Chen, *Nat. Mater.* **13**, 677 (2014).
- [8] H. Weng, C. Fang, Z. Fang, B. A. Bernevig, and X. Dai, *Phys. Rev. X* **5**, 011029 (2015).
- [9] S. Y. Xu, I. Belopolski, N. Alidoust, M. Neupane, G. Bian, C. Zhang, R. Sankar, G. Chang, Z. Yuan, C. C. Lee, S. M. Huang, H. Zheng, J. Ma, D. S. Sanchez, B. Wang, A. Bansil, F. Chou, P. P. Shibayev, H. Lin, S. Jia, and M. Z. Hasan, *Science* **349**, 613 (2015).
- [10] B. Q. Lv, H. M. Weng, B. B. Fu, X. P. Wang, H. Miao, J. Ma, P. Richard, X. C. Huang, L. X. Zhao, G. F. Chen, Z. Fang, X. Dai, T. Qian, and H. Ding, *Phys. Rev. X* **5**, 031013 (2015).
- [11] S.-Y. Xu, C. Liu, S. K. Kushwaha, R. Sankar, J. W. Krizan, I. Belopolski, M. Neupane, G. Bian, N. Alidoust, T. R. Chang, H. T. Jeng, C. Y. Huang, W. F. Tsai, H. Lin, P. P. Shibayev, F. C. Chou, R. J. Cava, and M. Z. Hasan, *Science* **347**, 294 (2015).
- [12] H. Weng, Y. Liang, Q. Xu, R. Yu, Z. Fang, X. Dai, and Y. Kawazoe, *Phys. Rev. B* **92**, 045108 (2015).
- [13] R. Yu, H. Weng, Z. Fang, X. Dai, and X. Hu, *Phys. Rev. Lett.* **115**, 036807 (2015).
- [14] G. Bian, T.-R. Chang, R. Sankar, S.-Y. Xu, H. Zheng, T. Neupert, C.-K. Chiu, S.-M. Huang, G. Chang, I. Belopolski, D. S. Sanchez, M. Neupane, N. Alidoust, C. Liu, B. Wang, H.-T. Jeng, A. Bansil, F. Chou, H. Lin, and M. Z. Hasan, *Nat. Commun.* **7**, 10556 (2016).
- [15] T. Liang, Q. Gibson, M. N. Ali, M. H. Liu, R. J. Cava, and N. P. Ong, *Nat. Mater.* **14**, 280 (2015).
- [16] C. Shekhar, A. K. Nayak, Y. Sun, M. Schmidt, M. Nicklas, I. Leermakers, U. Zeitler, Z. K. Liu, Y. L. Chen, W. Schnelle, J. Grin, C. Felser, and B. H. Yan, *Nat. Phys.* **11**, 645 (2015).
- [17] X. C. Huang, L. X. Zhao, Y. J. Long, P. P. Wang, D. Chen, Z. H. Yang, H. Liang, M. Q. Xue, H. M. Weng, Z. Fang, X. Dai, and G. F. Chen, *Phys. Rev. X* **5**, 031023 (2015).
- [18] J. Xiong, S. K. Kushwaha, T. Liang, J. W. Krizan, M. Hirschberger, W. Wang, R. J. Cava, and N. P. Ong, *Science* **350**, 413 (2015).
- [19] C. Fang, H. Weng, X. Dai, and Z. Fang, *Chin. Phys. B* **25**, 117106 (2016).
- [20] T. Bzdušek, Q. Wu, A. Rüegg, M. Sigrist, and A. A. Soluyanov, *Nature (London)* **538**, 75 (2016).
- [21] L. S. Xie, L. M. Schoop, E. M. Seibel, Q. D. Gibson, W. Xie, and R. J. Cava, *APL Mater.* **3**, 083602 (2015).
- [22] Y.-H. Chan, C.-K. Chiu, M. Y. Chou, and A. P. Schnyder, *Phys. Rev. B* **93**, 205132 (2016).
- [23] L. M. Schoop, M. N. Ali, C. Straßer, A. Topp, A. Varykhalov, D. Marchenko, V. Duppel, S. S. P. Parkin, B. V. Lotsch, and C. R. Ast, *Nat. Commun.* **7**, 11696 (2016).
- [24] J. Hu, Z. Tang, J. Liu, X. Liu, Y. Zhu, D. Graf, K. Myhro, S. Tran, C. N. Lau, J. Wei, and Z. Mao, *Phys. Rev. Lett.* **117**, 016602 (2016).

- [25] A. Yamakage, Y. Yamakawa, Y. Tanaka, and Y. Okamoto, *J. Phys. Soc. Jpn.* **85**, 013708 (2016).
- [26] D. Takane, K. Nakayama, S. Souma, T. Wada, Y. Okamoto, K. Takenaka, Y. Yamakawa, A. Yamakage, T. Mitsuhashi, K. Horiba, H. Kumigashira, T. Takahashi, and T. Sato, *npj Quantum Mater.* **3**, 1 (2018).
- [27] X.-B. Wang, X.-M. Ma, E. Emmanouilidou, B. Shen, C.-H. Hsu, C.-S. Zhou, Y. Zuo, R.-R. Song, S.-Y. Xu, G. Wang, L. Huang, N. Ni, and C. Liu, *Phys. Rev. B* **96**, 161112 (2017).
- [28] X. Zhang, Z.-M. Yu, X.-L. Sheng, H. Y. Yang, and S. A. Yang, *Phys. Rev. B* **95**, 235116 (2017).
- [29] X. Feng, C. Yue, Z. Song, Q. Wu, and B. Wen, *Phys. Rev. Mater.* **2**, 014202 (2017).
- [30] See Supplemental Material at <http://link.aps.org/supplemental/10.1103/PhysRevB.97.205105> for ZrB₂ single-crystal growth and first-principles calculation method; powder XRD pattern; MR at various temperatures, field, and current directions; two-band L-K formula fit of SdH QO with $\phi_B = 0$; and the fit of $\rho_{xx}(T, 0)$ at low temperature using the formula $\rho_0 + AT^n$.
- [31] T. M. Branscomb, and O. Hunter, Jr., *J. Appl. Phys.* **42**, 2309 (1971).
- [32] B. Fisher, K. B. Chashka, L. Patlagan, and G. M. Reisner, *Physica C* **384**, 1 (2003).
- [33] E. Forzania and K. Winzer, *Eur. Phys. J. B* **51**, 29 (2006).
- [34] J. M. Ziman, *Electrons and Phonons* (Clarendon Press, Oxford, 1960).
- [35] M. N. Ali, J. Xiong, S. Flynn, J. Tao, Q. D. Gibson, L. M. Schoop, T. Liang, N. Haldolaarachchige, M. Hirschberger, N. P. Ong, and R. J. Cava, *Nature (London)* **514**, 205 (2014).
- [36] F. F. Tafti, Q. D. Gibson, S. K. Kushwaha, N. Haldolaarachchige, and R. J. Cava, *Nat. Phys.* **12**, 272 (2016).
- [37] S. S. Sun, Q. Wang, P.-J. Guo, K. Liu, and H. C. Lei, *New J. Phys.* **18**, 082002 (2016).
- [38] J. Piper, *J. Phys. Chem. Solids* **27**, 1907 (1966).
- [39] A. Fawcztte, *Adv. Phys.* **13**, 139 (1964).
- [40] T. Tanaka, Y. Ishizawa, E. Bannai, and S. Kawai, *Solid State Commun.* **26**, 879 (1978).
- [41] V. B. Pluzhnikov, I. V. Svechkeev, A. V. Dukhnenko, A. V. Levchenko, V. B. Filippov, and A. Chopnik, *Low Temp. Phys.* **33**, 350 (2007).
- [42] D. Shoenberg, *Magnetic Oscillations in Metals* (Cambridge University Press, Cambridge, England, 1984).
- [43] I. M. Lifshitz and L. M. Kosevich, *Sov. Phys. JETP* **6**, 67 (1958).
- [44] O. Pavlosiuk, P. Swatek, and P. Wiśniewski, *Sci. Rep.* **6**, 38691 (2016).
- [45] G. P. Mikitik and Yu. V. Sharlai, *Phys. Rev. Lett.* **82**, 2147 (1999).
- [46] I. A. Luk'yanchuk and Y. Kopelevich, *Phys. Rev. Lett.* **93**, 166402 (2004).
- [47] F.-X. Xiang, X.-L. Wang, M. Veldhorst, S.-X. Dou, and M. S. Fuhrer, *Phys. Rev. B* **92**, 035123 (2015).
- [48] D. Rhodes, S. Das, Q. R. Zhang, B. Zeng, N. R. Pradhan, N. Kikugawa, E. Manousakis, and L. Balicas, *Phys. Rev. B* **92**, 125152 (2015).
- [49] R. Singha, A. K. Pariari, B. Satpati, and P. Mandal, *Proc. Natl. Acad. Sci. U.S.A.* **114**, 2468 (2017).
- [50] Y. L. Wang, L. R. Thoutam, Z. L. Xiao, J. Hu, S. Das, Z. Q. Mao, J. Wei, R. Divan, A. Luican-Mayer, G. W. Crabtree, and W. K. Kwok, *Phys. Rev. B* **92**, 180402(R) (2015).
- [51] P.-J. Guo, H.-C. Yang, B.-J. Zhang, K. Liu, and Z.-Y. Lu, *Phys. Rev. B* **93**, 235142 (2016).
- [52] D. V. Khveshchenko, *Phys. Rev. Lett.* **87**, 206401 (2001).